Chemosphere 288 (2022) 132584

Contents lists available at ScienceDirect

Chemosphere

journal homepage: www.elsevier.com/locate/chemosphere

Aptamer-functionalized and silver-coated polydopamine-copper hybrid nanoflower adsorbent embedded with magnetic nanoparticles for efficient mercury removal

Ho Kyeong Kim [a,b,1], Phuong Thy Nguyen [c,1], Moon Il Kim [c,*], Byoung Chan Kim [a,d,**]

[a] Center for Environment, Health and Welfare Research, Korea Institute of Science and Technology (KIST), Hwarangno 14-gil 5, Seongbuk-gu, Seoul, 02792, Republic of Korea
[b] Department of Chemical and Biological Engineering, Korea University, Seoul, 02841, Republic of Korea
[c] Department of BioNano Technology, Gachon University, Seongnam, Gyeonggi, 13120, Republic of Korea
[d] Division of Energy and Environment Technology, KIST School, University of Science and Technology (UST), Hwarangno 14-gil 5, Seongbuk-gu, Seoul, 02792, Republic of Korea

HIGHLIGHTS

- The aptamer hybrid nanoflower particles were synthesized to remove mercury ions.
- Thymine-rich Hg^{2+}-binding aptamers were functionalized to nanoflower particles.
- The aptamer hybrid nanoflower particles improved the performance of mercury ions adsorption.
- The maximum Hg^{2+} adsorption capacity of aptamer hybrid nanoflower was 1073.19 mg/g.
- The adsorption isotherm of aptamer hybrid nanoflower on Hg^{2+} followed the Dubinin–Radushkevich model.

GRAPHICAL ABSTRACT

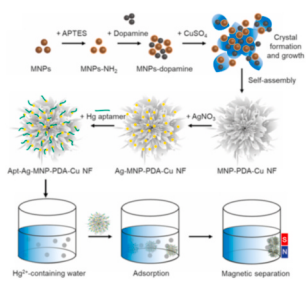

ARTICLE INFO

Handling Editor: Chang Min Park

Keywords:
Mercury removal
Hybrid nanoflowers
Adsorption
Magnetic separation
Aptamer

ABSTRACT

Mercury (Hg) emissions are increasing annually owing to rapid global industrialization. Hg poisoning can severely affect the human body owing to its persistence and bioaccumulation. In this study, hybrid nanoflowers (NFs) were synthesized by promoting the formation of primary copper-phosphate crystals coordinated with polydopamine (PDA) and Fe_3O_4 magnetic nanoparticles (MNPs), followed by coating with silver nanoparticles on the surface of the NFs (Ag-MNP-PDA-Cu NFs). The results suggest that the hierarchical structure of the NFs enabled a large surface area with nanosized pores, which were exploited for Hg adsorption. The adsorbed Hg ions could be further eliminated from the solution based on the magnetic characteristics of the NFs. Additionally, hybrid NFs functionalized with Hg^{2+}-binding aptamers (Apt-Ag-MNP-PDA-Cu NFs) were prepared based on the silver–sulfur interactions between the Ag-MNP-PDA-Cu NFs and thiol-modified aptamers. The performance of both adsorbents demonstrated that the immobilization of Hg^{2+}-binding aptamers significantly improved the

* Corresponding author.
** Corresponding author. Center for Environment, Health and Welfare Research, Korea Institute of Science and Technology (KIST), Hwarangno 14-gil 5, Seongbuk-gu, Seoul, 02792, Republic of Korea.
E-mail addresses: moonil@gachon.ac.kr (M.I. Kim), bchankim@kist.re.kr (B. Chan Kim).
[1] These authors contributed equally to this work.

https://doi.org/10.1016/j.chemosphere.2021.132584
Received 15 July 2021; Received in revised form 12 October 2021; Accepted 14 October 2021
Available online 19 October 2021
0045-6535/© 2021 Elsevier Ltd. All rights reserved.

elimination of Hg from solution. The Hg^{2+} adsorption isotherm of the Apt-Ag-MNP-PDA-Cu NFs followed the Dubinin–Radushkevich model, with a maximum adsorption capacity of 1073.19 mg/g. The Apt-Ag-MNP-PDA-Cu NFs adsorbed greater amounts of Hg^{2+} than the non-functionalized NFs at the same concentrations, which confirmed that the functionalization of Hg^{2+}-binding aptamers on the NFs improved the Hg^{2+} removal performance. The results suggest that Apt-Ag-MNP-PDA-Cu NFs could serve as an efficient Hg-removing adsorbent, possibly by providing binding sites for the formation of T-Hg^{2+}-T complexes.

1. Introduction

The amount of mercury (Hg) in ecosystems is increasing owing to the annually increasing emissions. A large amount of Hg is released owing to rapid industrialization via electricity generation, coal plant extensions, and biomass combustion. The increase in Hg levels in environmental water can lead to water pollution or accumulation in the human body, causing numerous severe health problems (Lamborg et al., 2014). Hg exists in aquatic environments in the form of ions, methyl mercury, and other inorganic mercurial compounds that are persistent and toxic to the environment and human health. Therefore, an efficient strategy must be developed to facilitate mercury removal from water sources, and several studies have been conducted to address this crucial issue (Boening, 2000; Obrist et al., 2018).

Various methods have been developed for Hg removal from aquatic environments, such as precipitation, ion exchange, biosorption, membrane technology, and adsorption. Among these methods, adsorption offers advantages such as cost-effectiveness, the use of simple equipment, and high effectiveness (Yu et al., 2016). Adsorbents for Hg removal have been developed by employing different types of materials, such as multi-walled carbon nanotubes (Hadavifar et al., 2014), activated carbon (Asasian et al., 2012), graphene oxide (Guo et al., 2016), TiO_2 nanoparticles (Binlin Dou, 2011), magnetic iron oxide nanoparticles (Parham et al., 2012), and MoS_2 nanoflowers on hydrogels (Ma et al., 2018). Among them, nanoparticles have been primarily utilized for heavy metal removal because of their large surface area, small size, and thermal stability. The morphology and functional groups on the surface of nanoparticles must be optimized to develop efficient nanoparticle-based adsorbents that can adequately remove heavy metals (Kataria and Garg, 2018). In particular, nanoparticles with flower-like morphologies exhibit enhanced heavy metal removal performance compared to those exhibited by nanoparticles with tubular- or wire-like morphologies. Moreover, nanoparticles with flower-like morphologies offer advantages such as ease of synthesis, low fabrication cost, and facile separation from the reacted solution after adsorption (Huang et al., 2012).

A unique strategy was recently proposed for preparing micrometer-sized hybrid particles possessing nanoscale architectures with a flower-like morphology (nanoflowers, NFs) using proteins and inorganic ions, such as copper (Ge et al., 2012). These hybrid structures have attracted attention owing to their ability to efficiently retain and stabilize the activity of entrapped protein molecules. Based on the significant improvement in the stability and activity of the entrapped proteins, these NFs have been extensively applied in biosensing (Kong et al., 2019; Tran et al., 2021), tryptic digestion (Lin et al., 2014), biodiesel production (Chung et al., 2018), and other enzymatic applications (Han et al., 2019; Nuan Feng, 2020). However, to the best of our knowledge, the structural superiority of hybrid NFs has not been thoroughly examined in terms of their applications. Besides, it has been highly beneficial to incorporate magnetic nanoparticles within the hybrid NFs, which enables facile magnetic separation and reutilization, resulting in cost-effective applications (Cheon et al., 2019; Meng et al., 2018; Nawaz et al., 2020). Therefore, hierarchically structured hybrid NFs with Fe_3O_4 magnetic nanoparticles (MNPs) incorporated within polydopamine (PDA)-copper hybrid NFs with a silver coating (Ag-MNP-PDA-Cu NFs) were developed. The hybrid NFs were first applied as adsorbents for mercury removal by conjugating aptamers on the surface of the Ag-MNP-PDA-Cu NFs.

Aptamers, which are synthetic oligonucleotides, have a specific affinity for target molecules, such as chemical compounds, proteins, and metal ions (Tuerk and Gold, 1990; Banerjee and Nilsen-Hamilton, 2013). Interactions between aptamers and target molecules, including van der Waals forces, hydrogen bonding, and hydrophobic interactions, allow the aptamer to bind specifically to the target molecule (Cai et al., 2018). For example, aptamers containing dominant thymine sequences are well known to bind specifically with Hg because Hg^{2+} ions combine with two thymines stably forming a thymine–Hg^{2+}–thymine complex (T–Hg^{2+}–T) (Ono and Togashi, 2004; Chun et al., 2018; Yuan et al., 2021). Thymine-rich aptamers have been applied as sensor probes for detecting Hg ions, although they are rarely used to remove Hg ions from aqueous solutions. In addition, aptamers can be easily modified with various functional groups and immobilized on nanomaterials such as gold nanoparticles and quantum dots (Zhang et al., 2013; Banerjee et al., 2016). In this study, thymine-rich aptamers with thiol residues were functionalized on the Ag-MNP-PDA-Cu NFs via specific interactions between Ag and the thiol residues on the aptamers (Gan et al., 2011). Thus, due to this strong silver-sulfur interaction, Hg ions captured by T-rich aptamers on the NFs are difficult to release in solution.

Owing to the embedded MNPs, the NFs with Hg ions that were adsorbed or captured by aptamers were readily separated from the solution using a magnet and efficiently reutilized. The large surface area coated with Ag resulted in the NFs possessing abundant sites for aptamer binding, consequently yielding high aptamer loading and enabling efficient removal of Hg ions.

2. Materials and methods

2.1. Materials

Hg^{2+} stock solution (1000 mg/L), sodium dodecyl sulfate (SDS), iron (III) chloride hexahydrate, iron(II) chloride tetrahydrate, dopamine hydrochloride, copper(II) sulfate pentahydrate, phosphate buffered saline (PBS), 3-aminopropyl triethoxysilane (APTES), silver nitrate, and dithiothreitol (DTT) were purchased from Sigma-Aldrich (USA). NAP-5 columns (Sephadex G-25 DNA grade) were purchased from GE Healthcare (Buckinghamshire, UK). Thiol-modified and non-thiol-modified Hg^{2+}-binding aptamers (5′ThioMC6-D/TTTTTTTTTT and TTTTTTTTTT, respectively) were synthesized by Integrated DNA Technologies (Coralville, IA, USA) and diluted with UltraPure™ DNase/RNase-free distilled water (Thermo Fisher Scientific). SDS, 1,5-diphenylthiocarbazone (dithizone; Alfa Aesar, USA), ethanol (Merck, Germany), and sulfuric acid (H_2SO_4; Jusei Chemical, Japan) were used for the spectrophotometric determination of Hg.

2.2. Synthesis of MNPs and amine-functionalized MNPs

MNPs were synthesized by a simple co-precipitation method (Lu et al., 2007). A mixture of $FeCl_2$ and $FeCl_3$ was first dissolved in water at a Fe^{3+}/Fe^{2+} ratio of 2:1, followed by the addition of sodium hydroxide solution (1 M) until the pH of the mixture reached 10. The mixture was subsequently heated at 80 °C for 40 min with stirring. The resultant MNPs were washed with deionized (DI) water and ethanol three times and dried at 70 °C under vacuum. Amine-functionalized MNPs were synthesized using a procedure reported by Gao et al. (2005). The MNPs

(5 g) were washed with methanol and suspended in 10 mL of methanol and toluene in a 1:1 vol ratio. APTES (10 μL, 3 mM) was subsequently added, followed by vigorous stirring at 80 °C for 20 h under a N_2 atmosphere. The obtained precipitate was washed with methanol via magnetic separation and subsequently dried under vacuum.

2.3. Synthesis of Ag-MNP-PDA-Cu NFs

MNP-PDA-Cu NFs were prepared according to our previously reported procedures, with certain modifications (Cheon et al., 2019). Briefly, amine-functionalized MNPs (0.1 mg/mL) and dopamine hydrochloride (0.1 mg/mL) were mixed in PBS buffer (10 mM, pH 7.4), followed by the addition of $CuSO_4$ (120 mM) and incubation at 22 °C for 3 d. The synthesized NFs (MNP-PDA-Cu NFs) were collected after incubation using a magnet and washed three times with DI water. The Ag-MNP-PDA-Cu NFs were synthesized by coating the as-synthesized NFs with silver crystals via incubation in $AgNO_3$ solution (0.02 mg/mL) for 5 h. The resultant NFs were separated using a magnet and washed with DI water three times. MNP-Cu NFs were prepared as a control by incubating amine-functionalized MNPs (0.1 mg/mL) in PBS buffer (10 mM, pH 7.4) without the addition of dopamine hydrochloride, followed by the aforementioned procedures.

2.4. Functionalization of Hg^{2+}-binding aptamers on the Ag-MNP-PDA-Cu NFs

The functionalization of the as-prepared Ag-MNP-PDA-Cu NFs with thiol-modified Hg^{2+}-binding aptamers (5′-thiol-TTTTTTTTTT-3′) is summarized. Prior to their use, thiol-modified Hg^{2+}-binding aptamers (100 μM) were mixed with DTT (2 M) in a 1:1 vol ratio and incubated for 20 min to ensure complete cleavage of disulfides, followed by purification using the NAP-5 columns to obtain SH-Hg^{2+}-binding aptamers. The conjugation of the SH-Hg^{2+}-binding aptamers on the Ag-MNP-PDA-Cu NFs was achieved by adding 10 μM SH-Hg^{2+}-binding aptamers to a 1 mg/mL NF solution; the mixture was incubated overnight, followed by a typical salt aging process. The aptamer-functionalized Ag-MNP-PDA-Cu NFs (Apt-Ag-MNP-PDA-Cu NFs) were subsequently collected using a magnet, washed three times, and resuspended in PBS buffer (0.1 M, pH 7.0).

2.5. Characterization of NFs

The MNP-Cu NFs, MNP-PDA-Cu NFs, Ag-MNP-PDA-Cu NFs, and Apt-Ag-MNP-PDA-Cu NFs were characterized by field emission scanning electron microscopy (FESEM; Magellan™ 400). The elemental composition of the NFs was analyzed using energy-dispersive X-ray spectroscopy (EDS; Bruker, Billerica, MA, USA). Magnetic properties were analyzed using a vibrating sample magnetometer (VSM, MPMS3-Evercool, Quantum Design). X-ray diffraction (XRD) analysis was conducted using a D/MAX-2500 setup (Rigaku Corporation, Tokyo, Japan); the synthesized NFs were washed with DI water and dried at 70 °C for 1 d prior to this analysis. Fourier-transform infrared spectroscopy (FT-IR) analysis of the as-prepared NFs was performed using an FT-IR spectrophotometer (FT/IR-4600, JASCO, Easton, MD). The specific surface area and pore size distribution were determined using nitrogen physisorption isotherms obtained using a physisorption analyzer (3Flex, Micromeritics, GA, USA) based on the Brunauer–Emmett–Teller (BET) and Barrett–Joyner–Halenda (BJH) methods. The encapsulation yield of the Hg^{2+}-binding aptamers conjugated to the NFs was calculated by measuring the amount of DNA in the supernatant using a NanoDrop 1000 system (Thermo Fisher Scientific). The weight percentage of the Hg^{2+}-binding aptamers conjugated to the NFs was calculated based on the encapsulation yield and weight of the powder.

2.6. Mercury adsorption on Apt-Ag-MNP-PDA-Cu NFs

A Hg(II) solution was prepared by diluting a Hg standard solution (1000 mg/L) with DI water. The adsorption capacities of the Apt-Ag-MNP-PDA-Cu NFs were determined by measuring the initial and final Hg(II) concentrations in the solution. For the adsorption kinetic study, each NF solution (100 μg/mL, 100 μL) was added to 400 μL solutions of Hg(II) with final concentrations of 0 and 10 mg/L. Subsequently, the mixtures were shaken on a thermomixer at 1200 rpm for different durations (5, 10, 30, 60, 90, 120, 180, and 240 min). The NFs were removed after 15 min using a magnet. The adsorbent and adsorbate were mixed to obtain the adsorption isotherm of the Apt-Ag-MNP-PDA-Cu NFs with a batch system so that the final Hg(II) concentrations in the mixtures were 0, 10, 20, 30, and 40 mg/L.

Each coexisting ion solution, such as Na^+, K^+, Mg^{2+}, Ca^{2+}, Al^{3+}, and Fe^{3+}, was added to the Hg ion solution so that the concentrations of other ions and Hg were 10 mg/L in the solution. The coexisting ions mixture sample was prepared to mix all coexisting ions with the Hg ion solution. The concentrations of all ions present in the solution were equal to 10 mg/L.

The Hg(II) concentration was determined by measuring the absorbance at 490 nm using a UV–vis spectrophotometer (Khan et al., 2005). A simple spectrophotometric method for Hg determination was modified to enable microvolume analysis. The sample solution (100 μL) was mixed with 500 μL of 0.6 M SDS, 100 μL of 1 M H_2SO_4, 100 μL of 1.95×10^{-4} M dithizone solution, and 100 μL DI water. The absorbance of the mixture was measured at 490 nm against a blank reagent. The standard points were 0, 1, 2, 5, and 10 mg/L of Hg(II) solution.

3. Results and discussion

3.1. Construction of Hg^{2+}-binding aptamers-functionalized Ag-MNP-PDA-Cu NFs

Multi-component hybrid NFs consisting of amine-rich PDA and copper with embedded MNPs, Ag-coated nanoparticles, and conjugated Hg^{2+}-binding aptamers were developed as new adsorbents for Hg removal, and the synthetic process is illustrated in Scheme 1. The addition of $CuSO_4$ to a PBS solution containing both dopamine and

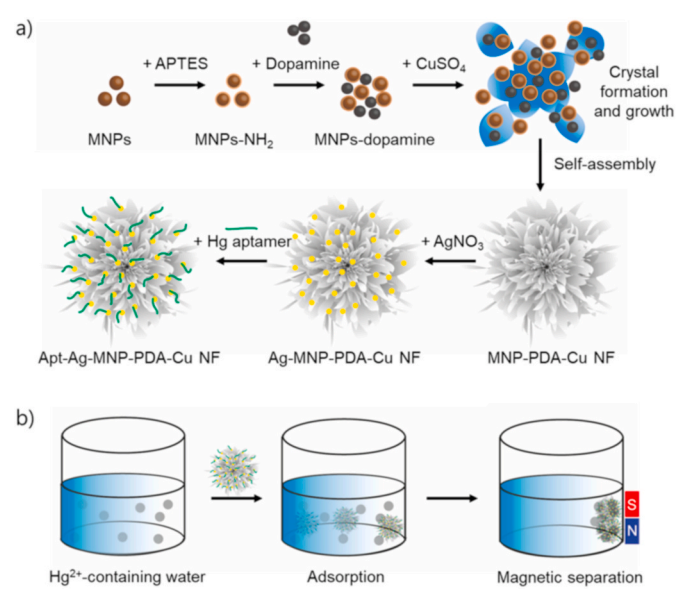

Scheme 1. Schematic representation of: (a) the construction of Apt-Ag-MNP-PDA-Cu NFs; and (b) their application for mercury removal via adsorption. Apt – aptamers, MNP – magnetic nanoparticles, PDA – polydopamine, NFs – hybrid nanoflowers.

amine-functionalized MNPs, resulted in interactions between Cu^{2+} ions and the amine moieties of PDA and the amine-functionalized MNPs, which promoted the formation of primary copper-phosphate crystals. Flower-shaped blooming was induced during 3 d of incubation via anisotropic growth and self-assembly of copper phosphate with PDA and amine-functionalized MNPs. $AgNO_3$ was subsequently added to enable reduction into silver nanoparticles (AgNPs) on the NF surface without the addition of a reducing agent, exploiting the reductive capability of PDA. PDA served as a green reductant for the formation and anchoring of AgNPs on the surface of NFs, as previously demonstrated (Yang et al., 2016). Thiol-modified Hg^{2+}-binding aptamers were subsequently added and conjugated to the AgNPs of the hybrid NFs based on interactions between Ag and the SH groups of the thiols of the aptamers. The high affinity of the Hg^{2+}-binding aptamer to Hg ions was expected to result in multi-component entrapping NFs (Apt-Ag-MNP-PDA-Cu NFs), which act as effective adsorbents for Hg removal.

The SEM images in Fig. 1 confirm the successful preparation of the synthesized MNP-Cu NFs, MNP-PDA-Cu NFs, Ag-MNP-PDA-Cu NFs, and Apt-Ag-MNP-PDA-Cu NFs, all of which exhibited flower-like hierarchical morphologies with a high surface-to-volume ratio. Notably, the petals of the NFs containing both MNPs and PDA, (MNP-PDA-Cu NFs, Ag-MNP-PDA-Cu NFs, and Apt-Ag-MNP-PDA-Cu NFs; Fig. 1 b–c) appeared to be more condensed compared to those of the MNP-Cu NFs, possibly because of the abundant active amine moieties of PDA.

The elemental composition of the Apt-Ag-MNP-PDA-Cu NFs was investigated using EDS mapping analysis (Fig. S1). The experimental results clearly demonstrate that the representative elements corresponding to copper phosphate (Cu and P), MNP (Fe), PDA (N), and AgNP (Ag) were distributed throughout the NFs. Furthermore, the surface area, pore volume, and average pore size of the Apt-Ag-MNP-PDA-Cu NFs were determined to be 58.26 m^2/g, 0.21 cm^3/g, and 14.65 nm, respectively, using the BET method, thereby confirming the presence of porous structures and high surface-to-volume ratio of the NFs (Fig. S2). VSM analysis demonstrated that both Ag-MNP-PDA-Cu NFs and Apt-Ag-MNP-PDA-Cu NFs have magnetic properties (20 emu/g) due to the presence of MNPs within their structures. The Apt-Ag-MNP-PDA-Cu NFs could be easily separated from the reaction solution by using external magnetic field, which facilitates their recycling and reutilization (Fig. S3).

FT-IR analysis of the MNP-Cu NFs, MNP-PDA-Cu NFs, Ag-MNP-PDA-Cu NFs, and Apt-Ag-MNP-PDA-Cu NFs were performed to characterize their chemical structures (Fig. 2a). The peaks appearing in the range of 989–1148 cm^{-1} in all the spectra originated from the stretching and vibration of P–O, which clearly confirmed the presence of phosphate groups (Mohammad et al., 2020). The absorption peaks at approximately 3400 and 586–555 cm^{-1} in all the spectra can be attributed to the hydroxyl groups and Fe–O bonds, which indicate the presence of MNPs (Cheon et al., 2019). The C═N vibration, aromatic ring C═C, and phenolic C–H stretching vibrations of PDA were responsible for the peaks at 1540, 1479, and 1291 cm^{-1}, respectively, which indicated the presence of PDA in the MNP-PDA-Cu NFs, Ag-MNP-PDA-Cu NFs, and Apt-Ag-MNP-PDA-Cu NFs; accordingly, these peaks did not appear in the spectrum of the MNP-Cu NFs due to the absence of PDA (Zangmeister et al., 2013; Kumar et al., 2014; Liu et al., 2017; Zhang et al., 2017).

XRD analysis was conducted to compare the crystal structures of the MNP-Cu NFs, MNP-PDA-Cu NFs, and Ag-MNP-PDA-Cu NFs (Fig. 2b). The XRD peaks of the three types of NFs appeared to match those of the standard crystal structures of $Cu_3(PO_4)\cdot 3H_2O$ (Joint Committee on Powder Diffraction Standards [JCPDS] 00-022-0548) and Fe_3O_4 (JCPDS 00-019-0629), which verifies the incorporation of the crystalline copper phosphates and MNPs into the NFs (Cheon et al., 2019). Moreover, the Ag-MNP-PDA-Cu NFs exhibited specific peaks at 38.0°, 44.5°, 64.7°, and 77.6°, which corresponded to the (111), (200), (220), and (311) crystalline planes of the Ag nanocrystals, respectively, thereby validating the successful functionalization of AgNPs on the MNP-PDA-Cu NFs (Zhang et al., 2017). The AgNPs on the surface of the Ag-MNP-PDA-Cu NFs assisted in the effective conjugation of the SH-Hg^{2+}-binding aptamers via silver–sulfur interactions between the AgNPs on the surface of the NFs and the thiol groups of the SH-Hg^{2+}-binding aptamers (Vidal et al., 2005). As expected, the encapsulation yield of the thiol-modified aptamers on the NFs was higher than that of the unmodified aptamers (Table S1). The weight percentage of Hg^{2+}-binding aptamers on the NFs was calculated to be 2.27%. All these results validate the successful

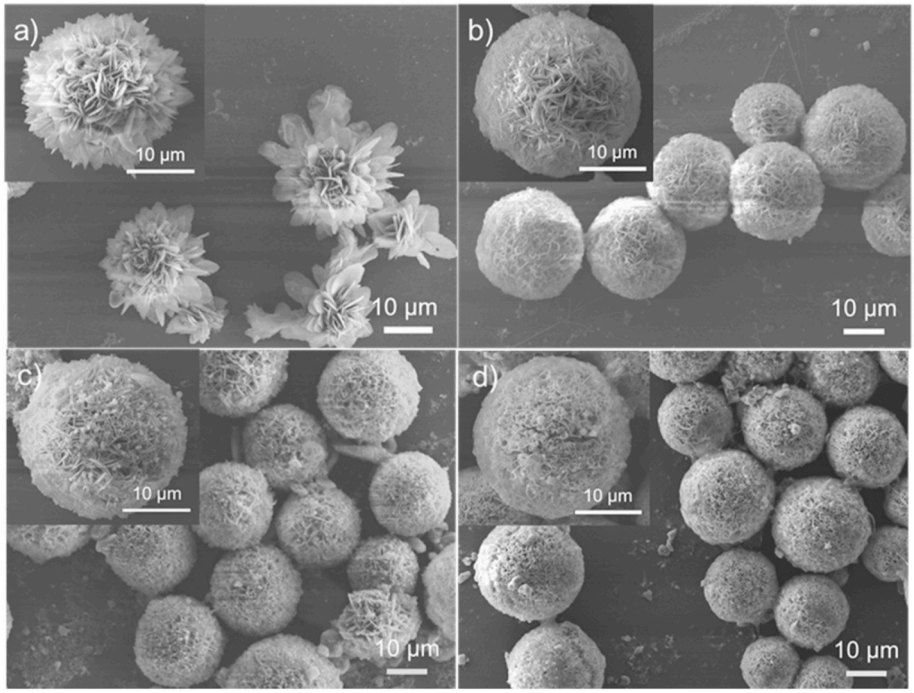

Fig. 1. Scanning electron microscopy (SEM) images of the: (a) copper magnetic nanoparticles MNP-Cu NFs, (b) MNP-PDA-Cu NFs, (c) Ag-MNP-PDA-Cu NFs, and (d) Apt-Ag-MNP-PDA-Cu NFs. Apt – aptamers, MNP – magnetic nanoparticles, PDA – polydopamine, NFs – hybrid nanoflowers.

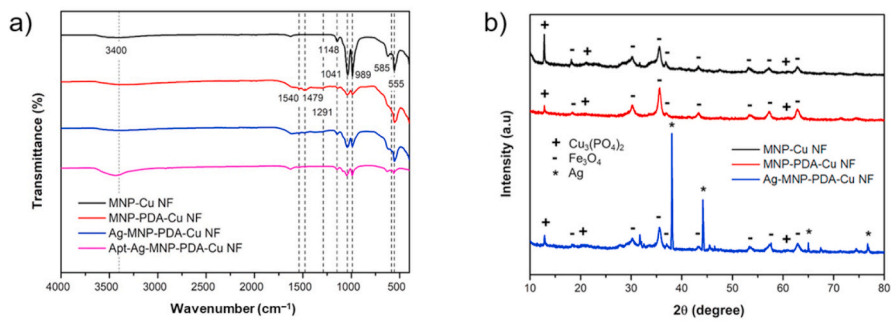

Fig. 2. (a) Fourier-transform infrared spectroscopy (FT-IR) spectra and (b) X-ray diffraction (XRD) patterns of the MNP-Cu NFs, MNP-PDA-Cu NFs, Ag-MNP-PDA-Cu NFs, and Apt-Ag-MNP-PDA-Cu NFs. Apt – aptamers, MNP – magnetic nanoparticles, PDA – polydopamine, NFs – hybrid nanoflowers.

preparation of the Apt-Ag-MNP-PDA-Cu NFs, which was achieved by incorporating multiple components such as the Hg^{2+}-binding aptamers, Ag, MNPs, PDA, and copper-phosphate crystals into the NFs.

3.2. Mercury adsorption using aptamer-functionalized Ag-MNP-PDA-Cu NFs

Adsorption kinetics studies were conducted to determine the equilibrium time and compare the Hg adsorption performance of aptamer-functionalized NFs (Apt-Ag-MNP-PDA-Cu NFs) with that of non-functionalized NFs (Ag-MNP-PDA-Cu NFs). The Hg adsorption process was performed with different contact times at room temperature (25 °C) and a pH of 2, where Apt-Ag-MNP-PDA-Cu NFs showed the best adsorption performance in a pilot study, as shown in Fig. S4. q_t, the amount of adsorbed Hg on the adsorbent at time t, was calculated using the following equation:

$$q_t = \frac{(C_0 - C_t) \times V}{m}, \quad (1)$$

where C_0 is the initial Hg concentration, C_t is the instantaneous Hg concentration, V is the reaction volume, and m is the mass of the adsorbent. Fig. 3 indicates that Ag-MNP-PDA-Cu NFs did not exhibit any adsorption capacity for Hg ions when the contact time was within 10 min. Rather, more than 30 min for incubation was required to obtain a reliable concentration value of adsorbed Hg on the Ag-MNP-PDA-Cu NFs. The adsorption capacity started to saturate, reaching 133.15 mg/g after 90 min of contact time. The equilibrium time for the adsorption of Apt-Ag-MNP-PDA-Cu NFs was 120 min (249.5 mg/g), which was 30 min longer than that of Ag-MNP-PDA-Cu NFs. However, Apt-Ag-MNP-PDA-Cu NFs adsorbed approximately twice the amount of Hg ions as Ag-MNP-PDA-Cu NFs at 120 min of contact time. In addition, the q_t value of Apt-Ag-MNP-PDA-Cu NFs increased sharply between 5 and 30 min of contact time compared to the plot of Ag-MNP-PDA-Cu NFs.

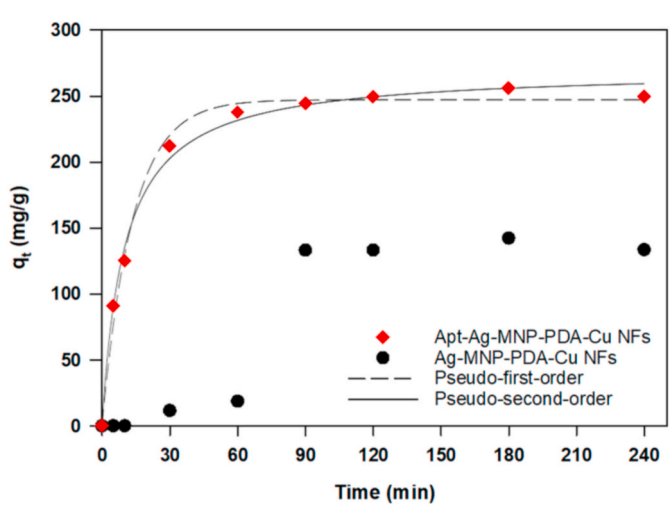

Fig. 3. Adsorption kinetics of the Ag-MNP-PDA-Cu NFs and Apt-Ag-MNP-PDA-Cu NFs.

Therefore, the functionalization of aptamers on adsorbents appeared to affect the adsorption performance of NFs. Thymine-rich DNA aptamers are known to have an affinity for Hg ions (Miyake et al., 2006; Xue et al., 2008). Hg^{2+} can bind to N_3 of thymidine and form the T-Hg-T complex, which is thermally more stable than Crick A–T (Xie et al., 2017). In addition, the presence of MNPs on the structure facilitates the separation of the NFs by a magnet without releasing Hg captured by the aptamers in the solution after adsorption.

In addition, Hg ions can be adsorbed onto silver nanoparticles embedded in the NF structure. Hg^{2+} ions strongly bond to the surface of AgNPs, forming Hg–Ag amalgam because Hg ions have a higher reduction potential than Ag ions (Fan et al., 2009; Vasileva et al., 2017). Most transition metal ions have lower reduction potentials than Ag ions; therefore, AgNPs selectively react with the Hg ions, and this redox reaction occurs spontaneously (Firdaus et al., 2017). Thus, both the Apt-Ag-MNP-PDA-Cu NFs and Ag-MNP-PDA-Cu NFs can remove Hg ions through chemisorption by AgNPs. This process occurs at AgNPs that do not react with thiol residues of Hg^{2+}-binding aptamers and remain on the surface of Apt-Ag-MNP-PDA-Cu NFs.

Moreover, two adsorption kinetic models were applied to understand the probable mechanism involved in Hg adsorption on Apt-Ag-MNP-PDA-Cu NF. The Lagergren model, also known as the pseudo-first-order model, assumes that the adsorption rate is directly proportional to the difference between the saturation concentration and the amount of adsorbate removed over time (Allen et al., 2005; Sahoo and Prelot, 2020). This model can be described as follows:

$$q_t = q_e(1 - \exp(-k_1 t)), \quad (2)$$

where q_e (mg/g) is the amount of adsorbate adsorbed on the adsorbent at equilibrium and k_1 is the equilibrium rate constant of the pseudo-first-order model. Kinetics commonly follow this model when adsorption proceeds via diffusion through the interface of the adsorbents.

The second is the pseudo-second-order model, which assumes that the rate-limiting step is chemical adsorption and that the adsorption rate depends on the adsorption capacity (Ho and McKay, 1998). This model can be expressed using the following equation:

$$q_t = q_e \frac{q_e k_2 t}{1 + q_e k_2 t}, \quad (3)$$

where k_2 is the equilibrium rate constant of the pseudo-second-order model. The parameters of the two kinetic models are summarized in Table 1.

The correlation coefficient (R^2) of the pseudo-second-order model was slightly higher than that of the pseudo-first-order model, although both were above 0.99 (Table 1). Considering that non-functionalized

Table 1
Kinetic parameters for Hg adsorption on Apt-Ag-MNP-PDA-Cu NFs.

Model	Equation	Parameters	R^2
Pseudo-first-order	$q_t = q_e(1 - \exp(-k_1 t))$	$k_1 = 0.0738$ $q_{e,\ cal} = 247.12$	0.9936
Pseudo-second-order	$q_t = q_e \frac{q_e k_2 t}{1 + q_e k_2 t}$	$k_2 = 0.00037$ $q_{e,\ cal} = 269.90$	0.9952

NFs did not exhibit adsorption capacities within 10 min of contact time, it could be assumed that chemical adsorption by Hg^{2+}-binding aptamers was primarily involved in Hg removal at the initial stage from 5 to 10 min of contact time. After the initial stage, Hg ions were adsorbed by diffusion on the hierarchical structure of the Apt-Ag-MNP-PDA-Cu NFs.

3.3. Effects of coexisting ions

The presence of other ions may have affected Hg adsorption on the adsorbent. In addition, cations such as Na^+ and Mg^{2+} are well known to contribute to the aptamer structure, which affect the binding affinity to a target molecule (Jiang et al., 2004). The adsorption capacity of Apt-Ag-MNP-PDA-Cu NFs was evaluated in the presence of other ions (Na^+, K^+, Mg^{2+}, Ca^{2+}, Al^{3+}, and Fe^{3+}). The results in Fig. 4 indicate that the adsorption capacity of the adsorbent exhibited no noticeable decline, even with coexisting ions. The q_e value decreased slightly in the presence of K^+, Mg^{2+}, and Ca^{2+}, whereas it increased when Na^+, Al^+, and Fe^{3+} were added. The coexisting ion mixture sample contained all other ions mentioned above at the same concentration as Hg ions (10 mg/L) that the concentration ratio of other ions to Hg ions was 6:1. The adsorption capacity of Apt-Ag-MNP-PDA-Cu NFs in the coexisting ion mixture sample was 247.7 mg/g, which was not different from that in the absence of coexisting ions (251.7 mg/g). These results demonstrate that Hg ions can be adsorbed on Apt-Ag-MNP-PDA-Cu regardless of the presence of coexisting ions.

3.4. Adsorption isotherm of aptamer-functionalized Ag-MNP-PDA-Cu NFs

A series of Hg ion solutions with concentrations of 0–40 mg/L were added to both adsorbents using a batch system under the optimized conditions to evaluate their corresponding adsorption capacities based on the adsorption isotherms (Fig. 5). Langmuir, Freundlich, and Dubinin–Radushkevich models were applied to analyze the experimental

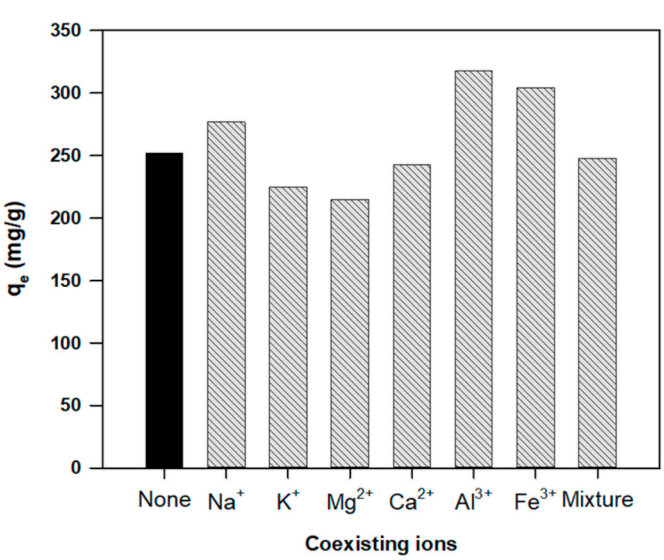

Fig. 4. Effect of coexisting ions on the mercury adsorption by Apt-Ag-MNP-PDA-Cu NFs.

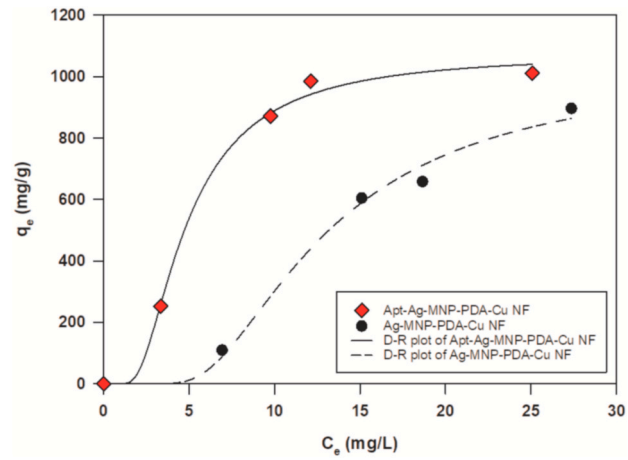

Fig. 5. Relationship between q_e (mg/g) and C_e (mg/L) at 25 °C. Dots represent experimental data of mercury adsorption on the hybrid NFs. D-R – Dubinin–Radushkevich isotherm model.

adsorption data (Ayawei et al., 2017). The calculated parameters of the three adsorption isotherm models are listed in Table 2.

The Langmuir model is based on monolayer adsorption and assumes the existence of finite adsorption sites in the adsorbent structure. The adsorption sites are energetically homogeneous, and there are no interactions between adjacent adsorbed molecules (Ajenifuja et al., 2017). Therefore, adsorption saturates when the adsorbate molecules occupy all the active sites. The Langmuir equation is expressed as follows:

$$q_e = \frac{Q_L K_L C_e}{1 + K_L C_e}, \tag{4}$$

where Q_L is the maximum adsorption capacity (mg/g), K_L is the Langmuir constant (L/mg), and C_e is the equilibrium concentration. The equilibrium adsorption capacity (q_e) was calculated using the following equation:

$$q_e = \frac{(C_0 - C_e) \times V}{m}, \tag{5}$$

where C_0 is the initial concentration of the adsorbate, C_e is the equilibrium concentration, V is the reaction volume, and m is the mass of the adsorbent. Table 2 shows that the Langmuir correlation coefficients (R^2) of both adsorbents were <0.96; moreover, the Q_L value of the Ag-MNP-PDA-Cu NFs was not available. These results demonstrate that Hg adsorption by the hybrid NFs did not follow the Langmuir model.

The Freundlich isotherm is an empirical adsorption model used to describe the adsorption occurring on heterogeneous surfaces of an

Table 2
Parameters of the Langmuir, Freundlich, and Dubinin–Radushkevich isotherm models for Hg(II) adsorption by each adsorbent.

Adsorption isotherm model	Parameter	Adsorbent	
		Apt-Ag-MNP-PDA-Cu NF	Ag-MNP-PDA-Cu NF
Langmuir	Q_L (mg/g)	1487.87	23,433.33
	K_L	0.115	0.0015
	R^2	0.936	0.956
Freundlich	K_F	266.83	30.25
	n	2.228	0.963
	R^2	0.882	0.956
Dubinin–Radushkevich	Q_{DR} (mg/g)	1073.19	1027.75
	K_{DR}	3.371	21.954
	R^2	0.997	0.992

adsorbent. The isotherm is expressed as follows:

$$q_e = K_f C_e^{\frac{1}{n}}, \quad (6)$$

where K_f and n are constants that represent the adsorption capacity and intensity, respectively. Table 2 shows that the R^2 of the Apt-Ag-MNP-PDA-Cu NFs corresponding to the Freundlich model was 0.882, whereas that of the Ag-MNP-PDA-Cu NFs was 0.956. These values were lower than those obtained using the Langmuir model; therefore, it is difficult to describe the interaction between Hg ions and the adsorbent, even with the Freundlich model. In addition, this model does not predict the maximum adsorption capacity. However, the q_e values in the plot corresponding to the Apt-Ag-MNP-PDA-Cu-NFs tended to be saturated (Fig. 5). Therefore, a more accurate adsorption model must be considered to elucidate this tendency.

The adsorption plots of the Apt-Ag-MNP-PDA-Cu NFs and Ag-MNP-PDA-Cu NFs exhibited *S*-shaped curves; therefore, a precise evaluation based on the Langmuir and Freundlich isotherm models was challenging. Therefore, the Dubinin–Radushkevich (D-R) isotherm model was subsequently used to evaluate the adsorption capacity. The D-R model can be applied to heterogeneous surface materials with microporous structures that follow the pore-filling mechanism (Wang and Guo, 2020). The D-R isotherm equation is expressed as follows:

$$q_e = Q_{DR} \exp\left(- K_{DR} \left[RT \ \ln\left(1 + \frac{1}{C_e}\right)\right]^2\right), \quad (7)$$

where Q_{DR} is the maximum capacity of the adsorbent (mg/g), R is the ideal gas constant (8.314 J/mol·K), and T is the absolute temperature (K). K_{DR} is the D-R isotherm constant (mol^2/kJ^2). Table 2 shows that the R^2 values of the D-R model for Hg^{2+} adsorption by the Apt-Ag-MNP-PDA-Cu NFs and Ag-MNP-PDA-Cu NFs were 0.997 and 0.992, respectively; these were the highest values among the adsorption isotherm models. These results suggest that both adsorbents have heterogeneous surfaces and adsorb Hg ions via a pore-filling mechanism derived from their hierarchical structure. Moreover, the maximum capacity (Q_{DR}) of the Apt-Ag-MNP-PDA-Cu NF adsorbent was 1073.19 mg/g, which was higher than that of the Ag-MNP-PDA-Cu NFs (1027.75 mg/g). The maximum adsorption capacities (Q_{max}) of the previously reported adsorbents are listed in Table 3. The Q_{max} values of the aptamer-functionalized NFs obtained herein are comparable to those of other types of adsorbents used for Hg removal.

In addition, the C_e values of the Apt-Ag-MNP-PDA-Cu NFs on Hg adsorption were lower than those of the non-functionalized NFs (Fig. 5), which proves that the Apt-Ag-MNP-PDA-Cu NFs adsorbed a greater amount of Hg^{2+} than that by the non-functionalized NFs at the same Hg^{2+} concentrations. This indicates that the functionalization of Hg^{2+}-binding aptamers provides active sites for the NFs, resulting in an increase in the binding affinity with the adsorbate and a maximum adsorption capacity comparable to that of the non-functionalized NFs.

4. Conclusions

Hybrid NFs composed of MNPs, PDA, AgNPs, and thymine-rich Hg^{2+}-binding aptamers have been successfully developed for Hg removal. The large surface-to-volume ratio of the NFs facilitated high performance for Hg removal via an adsorption mechanism based on pore-filling. Hg ions were confirmed to be adsorbed in the pores of the NFs or combined with the thymine of the aptamers immobilized on the NFs, which could be readily removed via magnetic separation. The Hg adsorption isotherms of both the Apt-Ag-MNP-PDA-Cu NF and Ag-MNP-PDA-Cu NF adsorbents followed the Dubinin–Radushkevich model. The adsorption capacity of the Apt-Ag-MNP-PDA-Cu NFs showed increases in the maximum capacity and binding affinity compared to those of the Ag-MNP-PDA-Cu NFs. Immobilization of Hg-binding aptamers on NFs was found to improve Hg adsorption performance.

Table 3
Comparison of the maximum adsorption capacity (Q_{max}) of the aptamer-functionalized hybrid NFs with that of previously reported adsorbents.

Adsorbent	Q_{max} (mg/g)	Reference
Functionalized multi-walled carbon nanotubes	84.66	Hadavifar et al. (2014)
Activated carbon	141	Asasian et al. (2012)
Walnut shells	151.5	Zabihi et al. (2010)
MoS_2 NFs anchored on PVA-5	2165	Ma et al. (2018)
Magnetic mesoporous silica nanoparticles	538.9	Mehdinia et al. (2015)
Magnetic graphene oxide composite	71.3	Guo et al. (2016)
Titanate nanoflowers	454.55	Liu et al. (2015)
Mesoporous conjugate adsorbent	172.61	Abbas et al. (2018)
Aptamer-functionalized hybrid nanoflowers	1073.19	Present study

Declaration of competing interest

The authors declare that they have no known competing financial interests or personal relationships that could have appeared to influence the work reported in this paper.

Acknowledgments

This study was supported by a National Research Foundation of Korea (NRF) grant funded by the Korean government (Ministry of Science and ICT [NRF-2019R1A2C1087459] and the Basic Science Research Program through the NRF funded by the Ministry of Education (Grant No. 2021R1A6A1A03038996). This study was also supported by the Korea Institute of Science and Technology (KIST) Institutional Research Program (2E31281 and 2E31371).

Appendix A. Supplementary data

Supplementary data to this article can be found online at https://doi.org/10.1016/j.chemosphere.2021.132584.

Credit author statement

Ho Kyeong Kim and Phuong Thy Nguyen: Writing – original draft, Investigation, Methodology, Data curation. **Moon Il Kim:** Conceptualization, Writing – review & editing, Supervision. **Byoung Chan Kim:** Conceptualization, Writing – review & editing, Supervision.

References

Abbas, K., Znad, H., Awual, M.R., 2018. A ligand anchored conjugate adsorbent for effective mercury(II) detection and removal from aqueous media. Chem. Eng. J. 334, 432–443.
Ajenifuja, E., Ajao, J.A., Ajayi, E.O.B., 2017. Adsorption isotherm studies of Cu (II) and Co (II) in high concentration aqueous solutions on photocatalytically modified diatomaceous ceramic adsorbents. Appl. Water. Sci. 7, 3793–3801.
Allen, S.J., Gan, Q., Matthews, R., Johnson, P.A., 2005. Kinetic modeling of the adsorption of basic dyes by kudzu. J. Colloid Interface Sci. 286, 101–109.
Asasian, N., Kaghazchi, T., Soleimani, M., 2012. Elimination of mercury by adsorption onto activated carbon prepared from the biomass material. J. Ind. Eng. Chem. 18, 283–289.
Ayawei, N., Ebelegi, A.N., Wankasi, D., 2017. Modelling and interpretation of adsorption isotherms. J. Chem. 2017 1–11.
Banerjee, A., Pons, T., Lequeux, N., Dubertret, B., 2016. Quantum dots–DNA bioconjugates: synthesis to applications. Interface Focus 6, 20160064.
Banerjee, J., Nilsen-Hamilton, M., 2013. Aptamers: multifunctional molecules for biomedical research. J. Mol. Med. (Berl) 91, 1333–1342.
Binlin Dou, V.D., Pan, Weiguo, Chen, Bingbing, 2011. Removal of aqueous toxic Hg(II) by synthesized TiO_2 nanoparticles and TiO_2/montmorillonite. Chem. Eng. J. 166, 631–638.
Boening, D.W., 2000. Ecological effects, transport, and fate of mercury: a general review. Chemosphere 40, 1335–1351.
Cai, S., Yan, J., Xiong, H., Liu, Y., Peng, D., Liu, Z., 2018. Investigations on the interface of nucleic acid aptamers and binding targets. Analyst 143, 5317–5338.

Cheon, H.J., Adhikari, M.D., Chung, M., Tran, T.D., Kim, J., Kim, M.I., 2019. Magnetic nanoparticles-embedded enzyme-inorganic hybrid nanoflowers with enhanced peroxidase-like activity and substrate channeling for glucose biosensing. Adv. Healthc. Mater. 8, 1801507.
Chun, H.J., Kim, S., Han, Y.D., Kim, D.W., Kim, K.R., Kim, H.-S., Kim, J.-H., Yoon, H.C., 2018. Water-soluble mercury ion sensing based on the thymine-Hg^{2+}-thymine base pair using retroreflective janus particle as an optical signaling probe. Biosens. Bioelectron. 104, 138–144.
Chung, M., Nguyen, T.L., Tran, T.Q.N., Yoon, H.H., Kim, I.T., Kim, M.I., 2018. Ultrarapid sonochemical synthesis of enzyme-incorporated copper nanoflowers and their application to mediatorless glucose biofuel cell. Appl. Surf. Sci. 429, 203–209.
Fan, Y., Liu, Z., Wang, L., Zhan, J., 2009. Synthesis of starch-stabilized Ag nanoparticles and Hg^{2+} recognition in aqueous media. Nanoscale Res. Lett. 4, 1230–1235.
Firdaus, M.L., Fitriani, I., Wyantuti, S., Hartati, Y.W., Khaydarov, R., McAlister, J.A., Obata, H., Gamo, T., 2017. Colorimetric detection of mercury(II) ion in aqueous solution using silver nanoparticles. Anal. Sci. 33, 831–837.
Gan, W., Xu, B., Dai, H.-L., 2011. Activation of thiols at a silver nanoparticle surface. Angew. Chem. Int. Ed. 50, 6622–6625.
Gao, F., Pan, B.-F., Zheng, W.-M., Ao, L.-M., Gu, H.-C., 2005. Study of streptavidin coated onto PAMAM dendrimer modified magnetite nanoparticles. J. Magn. Magn Mater. 293, 48–54.
Ge, J., Lei, J., Zare, R.N., 2012. Protein–inorganic hybrid nanoflowers. Nat. Nanotechnol. 7, 428–432.
Guo, Y., Deng, J., Zhu, J., Zhou, X., Bai, R., 2016. Removal of mercury(ii) and methylene blue from a wastewater environment with magnetic graphene oxide: adsorption kinetics, isotherms and mechanism. RSC Adv. 6, 82523–82536.
Hadavifar, M., Bahramifar, N., Younesi, H., Li, Q., 2014. Adsorption of mercury ions from synthetic and real wastewater aqueous solution by functionalized multi-walled carbon nanotube with both amino and thiolated groups. Chem. Eng. J. 237, 217–228.
Han, J., Luo, P., Wang, L., Li, C., Mao, Y., Wang, Y., 2019. Construction of magnetic nanoflower biocatalytic system with enhanced enzymatic performance by biomineralization and its application for bisphenol A removal. J. Hazard Mater. 380, 120901.
Ho, Y.S., McKay, G., 1998. Kinetic models for the sorption of dye from aqueous solution by wood. Process Saf. Environ. Protect. 76, 183–191.
Huang, J., Cao, Y., Liu, Z., Deng, Z., Tang, F., Wang, W., 2012. Efficient removal of heavy metal ions from water system by titanate nanoflowers. Chem. Eng. J. 180, 75–80.
Jiang, Y., Wang, J., Fang, X., Baia, C., 2004. Study of the effect of metal ion on the specific interaction between protein and aptamer by atomic force microscopy. J. Nanosci. Nanotechnol. 4, 611–615.
Kataria, N., Garg, V.K., 2018. Optimization of Pb (II) and Cd (II) adsorption onto ZnO nanoflowers using central composite design: isotherms and kinetics modelling. J. Mol. Liq. 271, 228–239.
Khan, H., Ahmed, M.J., Bhanger, M.I., 2005. A simple spectrophotometric determination of trace level mercury using 1,5-diphenylthiocarbazone solubilized in micelle. Anal. Sci. 21, 507–512.
Kong, D., Jin, R., Zhao, X., Li, H., Yan, X., Liu, F., Sun, P., Gao, Y., Liang, X., Lin, Y., 2019. Protein–inorganic hybrid nanoflower-rooted agarose hydrogel platform for point-of-care detection of acetylcholine. ACS Appl. Mater. Interfaces 11, 11857–11864.
Kumar, T.N., Sivabalan, S., Chandrasekaran, N., Phani, K.L.N., 2014. Ferrocene-functionalized polydopamine as a novel redox matrix for H_2O_2 oxidation. J. Mater. Chem. B 2, 6081–6088.
Lamborg, C.H., Hammerschmidt, C.R., Bowman, K.L., Swarr, G.J., Munson, K.M., Ohnemus, D.C., Lam, P.J., Heimbürger, L.-E., Rijkenberg, M.J.A., Saito, M.A., 2014. A global ocean inventory of anthropogenic mercury based on water column measurements. Nature 512, 65–68.
Lin, Z., Xiao, Y., Wang, L., Yin, Y., Zheng, J., Yang, H., Chen, G., 2014. Facile synthesis of enzyme–inorganic hybrid nanoflowers and their application as an immobilized trypsin reactor for highly efficient protein digestion. RSC Adv. 4, 13888–13891.
Liu, S., Qileng, A., Huang, J., Gao, Q., Liu, Y., 2017. Polydopamine as a bridge to decorate monodisperse gold nanoparticles on Fe_3O_4 nanoclusters for the catalytic reduction of 4-nitrophenol. RSC Adv. 7, 45545–45551.
Liu, W., Zhao, X., Wang, T., Fu, J., Ni, J., 2015. Selective and irreversible adsorption of mercury(ii) from aqueous solution by a flower-like titanate nanomaterial. J. Mater. Chem. 3, 17676–17684.
Lu, A.H., Salabas, E.e.L., Schüth, F., 2007. Magnetic nanoparticles: synthesis, protection, functionalization, and application. Angew. Chem. Int. Ed. 46, 1222–1244.
Ma, C.-B., Du, Y., Du, B., Wang, H., Wang, E., 2018. Investigation of an eco-friendly aerogel as a substrate for the immobilization of MoS_2 nanoflowers for removal of mercury species from aqueous solutions. J. Colloid Interface Sci. 525, 251–259.
Mehdinia, A., Akbari, M., Baradaran Kayyal, T., Azad, M., 2015. High-efficient mercury removal from environmental water samples using di-thio grafted on magnetic mesoporous silica nanoparticles. Environ. Sci. Pollut. Res. Int. 22, 2155–2165.
Meng, C., Zhikun, W., Qiang, L., Chunling, L., Shuangqing, S., Songqing, H., 2018. Preparation of amino-functionalized Fe_3O_4@mSiO_2 core-shell magnetic nanoparticles and their application for aqueous Fe^{3+} removal. J. Hazard Mater. 341, 198–206.
Miyake, Y., Togashi, H., Tashiro, M., Yamaguchi, H., Oda, S., Kudo, M., Tanaka, Y., Kondo, Y., Sawa, R., Fujimoto, T., Machinami, T., Ono, A., 2006. $Mercury^{II}$-mediated formation of thymine−Hg^{II}−thymine base pairs in DNA duplexes. J. Am. Chem. Soc. 128, 2172–2173.
Mohammad, M., Ahmadpoor, F., Shojaosadati, S.A., 2020. Mussel-inspired magnetic nanoflowers as an effective nanozyme and antimicrobial agent for biosensing and catalytic reduction of organic dyes. ACS Omega 5, 18766–18777.
Nawaz, T., Zulfiqar, S., Sarwar, M.I., Iqbal, M., 2020. Synthesis of diglycolic acid functionalized core-shell silica coated Fe_3O_4 nanomaterials for magnetic extraction of Pb (II) and Cr (VI) ions. Sci. Rep. 10 (1), 1–13.
Nuan Feng, H.Z., Yao, Li, Liu, Yangkaixi, Xu, Longquan, Wang, Yi, Xu, Fei, Tian, Jing, 2020. A novel catalytic material for hydrolyzing cow's milk allergenic proteins: papain-$Cu_3(PO_4)_2 \cdot 3H_2O$-magnetic nanoflowers. Food Chem. 311, 125911.
Obrist, D., Kirk, J.L., Zhang, L., Sunderland, E.M., Jiskra, M., Selin, N.E., 2018. A review of global environmental mercury processes in response to human and natural perturbations: changes of emissions, climate, and land use. Ambio 47, 116–140.
Ono, A., Togashi, H., 2004. Highly selective oligonucleotide-based sensor for mercury (II) in aqueous solutions. Angew. Chem. Int. Ed. 43, 4300–4302.
Parham, H., Zargar, B., Shiralipour, R., 2012. Fast and efficient removal of mercury from water samples using magnetic iron oxide nanoparticles modified with 2-mercaptobenzothiazole. J. Hazard Mater. 205–206, 94–100.
Sahoo, T.R., Prelot, B., 2020. Chapter 7 - adsorption processes for the removal of contaminants from wastewater: the perspective role of nanomaterials and nanotechnology. In: Bonelli, B., Freyria, F.S., Rossetti, I., Sethi, R. (Eds.), Nanomaterials for the Detection and Removal of Wastewater Pollutants. Elsevier, pp. 161–222.
Tran, T.D., Nguyen, P.T., Le, T.N., Kim, M.I., 2021. DNA-copper hybrid nanoflowers as efficient laccase mimics for colorimetric detection of phenolic compounds in paper microfluidic devices. Biosens. Bioelectron. 182, 113187.
Tuerk, C., Gold, L., 1990. Systematic evolution of ligands by exponential enrichment: RNA ligands to bacteriophage T4 DNA polymerase. Science 249, 505–510.
Vasileva, P., Alexandrova, T., Karadjova, I., 2017. Application of starch-stabilized silver nanoparticles as a colorimetric sensor for mercury(II) in 0.005mol/Lnitric acid. J . Chem .2017 1–9.
Vidal Jr., B.C., Deivaraj, T.C., Yang, J., Too, H.-P., Chow, G.-M., Gan, L.M., Lee, J.Y., 2005. Stability and hybridization-driven aggregation of silver nanoparticle–oligonucleotide conjugates. New J. Chem. 29, 812–816.
Wang, J., Guo, X., 2020. Adsorption isotherm models: classification, physical meaning, application and solving method. Chemosphere 258, 127279.
Xie, M., Zhang, K., Zhu, F., Wu, H., Zou, P., 2017. Strategy for the detection of mercury ions by using exonuclease III-aided target recycling. RSC Adv. 7, 50420–50424.
Xue, X., Wang, F., Liu, X., 2008. One-step, room temperature, colorimetric detection of mercury (Hg^{2+}) using DNA/nanoparticle conjugates. J. Am. Chem. Soc. 130, 3244–3245.
Yang, Z., Wu, Y., Wang, J., Cao, B., Tang, C.Y., 2016. In situ reduction of silver by polydopamine: a novel antimicrobial modification of a thin-film composite polyamide membrane. Environ. Sci. Technol. 50, 9543–9550.
Yu, J.-G., Yue, B.-Y., Wu, X.-W., Liu, Q., Jiao, F.-P., Jiang, X.-Y., Chen, X.-Q., 2016. Removal of mercury by adsorption: a review. Environ. Sci. Pollut. Res. Int. 23, 5056–5076.
Yuan, H., Sun, G., Peng, W., Ji, W., Chu, S., Liu, Q., Liang, Y., 2021. Thymine-functionalized gold aanoparticles (Au NPs) for a highly sensitive fiber-optic surface plasmon resonance mercury ion nanosensor. Nanomaterials 11, 397.
Zabihi, M., Haghighi Asl, A., Ahmadpour, A., 2010. Studies on adsorption of mercury from aqueous solution on activated carbons prepared from walnut shell. J. Hazard Mater. 174, 251–256.
Zangmeister, R.A., Morris, T.A., Tarlov, M.J., 2013. Characterization of polydopamine thin films deposited at short times by autoxidation of dopamine. Langmuir 29, 8619–8628.
Zhang, J., Liu, B., Liu, H., Zhang, X., Tan, W., 2013. Aptamer-conjugated gold nanoparticles for bioanalysis. Nanomedicine 8, 983–993.
Zhang, M., Peltier, R., Zhang, M., Lu, H., Bian, H., Li, Y., Xu, Z., Shen, Y., Sun, H., Wang, Z., 2017. In situ reduction of silver nanoparticles on hybrid polydopamine–copper phosphate nanoflowers with enhanced antimicrobial activity. J. Mater. Chem. B 5, 5311–5317.